24th EUROPEAN ROTORCRAFT FORUM

Marseilles, France - 15th-17th September 1998

A STUDY ON THE VORTICAL FLOW BEHAVIOR OF THE ROTOR BLADE

Référence : AE15

Choong Mo Yang and Je Hyun Baek
Department of Mechanical Engineering, Pohang University of Science and Technology
Hyoja-dong San 31, Pohang 790-784, Korea

ABSTRACT

Three-dimensional tip vortices of a wing in subsonic flows were analyzed with Euler equation solver using TVD scheme. The code was applied to the three dimensional fixed/rotary wing model with NACA0012 airfoil cross-section at various Mach numbers and angles of attack. With fixed wing, three kinds of inflow models were applied to show the individual effects of tip and rotation of rotor blade. With rotary wing, half-cylinderical rotating coordinate system with shear inflow was used to simulate the flow around the helicopter rotor, and the results was compared with those of fixed wings.

1. Nomenclature

F, G, H	inviscid flux vectors in Cartesian coordinate
J	Jacobian of coordinate transformation
Q	vector of conservative variables
R	residual
e	total energy per unit volume
p	pressure
u, v, w	Cartesian velocity in x, y, z direction
x, y, z	Cartesian coordinate
γ	ratio of specific heat
ξ, η, ζ	transformed coordinate
ϵ	entropy correction parameter
δ	difference operator
Γ	metric terms at cell interface
Λ	diagonal matrix of eigenvalue
ρ	density
i, j, k	cell index
L, R	left and right states at cell interface

2. Introduction

The prediction of the flow field over helicopter rotor blade is of great importance in the design and the development of new helicopter. Especially, the three-dimensional vortical wake (tip vortex), which is formed at the blade tip and shedded downward, has dominant influences on the aerodynamic characteristics in hovering and forward flight of a helicopter. The two features, in general, of the tip vortex should be considered properly in the analysis : (i) the contraction of the helical wakes as it extends in the axial direction below the rotor (i.e. wake contraction), (ii) the interaction between the vortex from one blade and flow fields of another following blade(i.e. blade-vortex interaction). Thses researches on initial roll-up phenomena of the concentrated vortex and the geometrical dependency of the blades will be able to modify the structure of the vortex to minimize the undesirable effects.

Various studies have been carried out by many researchers in the aerodynamic analysis of the helicopter rotor such as the momentum (energy) method by Rankine(1865) and Froude(1889), the vortex lattice method and the lifting surface method based on the potential and vortex theory, the methods using the transonic small disturbance equations and advanced full potential equations. However, unlike the Euler and Navier-Stokes equations, these equations cannot take into account the transport of vorticity, the roll-up of the wake following the blade and contraction of tip vortex past the blade, so they are less perfect model for the prediction of aerodynamic loads on rotor blades.

In order to be more powerful aerodynamic analysis tool for rotor blades, it must be able to consider the effect of viscosity, such as wake formation and blade stall, which are important for an even moderate operating conditions. Since the computing power has been increased progressively over the last two decades, the analysis of helicopter rotor flows in hover and forward flight has progressed from the solution of transonic small perturbation equations and full potential equations to that of Euler equations and more recently to that of Navier-Stokes equations.

The recent numerical simulation of the flow in the tip region of a transonic swept wing was performed by Mansour(1985), and by Kaynak et al.(1987) extended to three-dimensional shock-induced seperation using a multiblock Euler/Navier-Stokes zonal method. Later Srinivasan have extended the simulation of the flow-filed and the vortex-formation around the wing tip region to the transonic flow.

The three-dimensional flow field around a helicopter rotor blade can be characterized mainly in a tip vortex generated at the tip of a rotor blade and a rotating effect by the rotation of the rotor. The tip vortex generated in the backward vortex of a fixed wing or of a helicopter rotor blade has a great importance with a aerodynamical view. Since this tip vortex generally occurs in a complex three-dimensional seperating flow which is difficult to analize, most theoritical or experimental researchers have been trying to understand qualitatively the structure of a vorticity transport from a boundary layer near the wing surface to trailing concentrated vortex. The tip vortex is known to cause not only a flow instability such as a sudden decrease of a induced drag or a stall in boundary layer but also acoustic noise. Especially in the rotating blades such as propellers or helicopter rotors, more complex vortical wake is occurred by the interaction of following blade than the fixed wing. Figure 1, which was drawn by Wake(1987) in his paper, shows the schematic diagram of the same example of of the tip vortex and wake around the rotor blade with the computational domain.

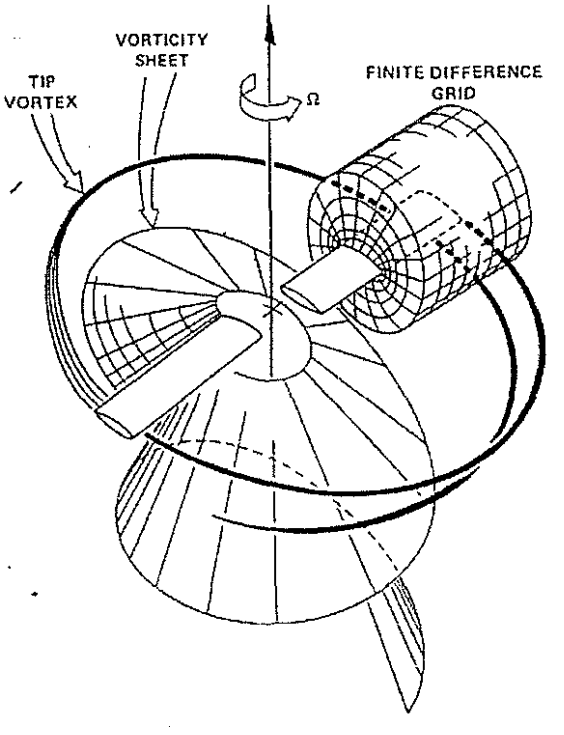

Fig.1: Schematic diagram of wake and tip vortex

In the present study, as a step to develop solution technique for the flowfield around a helicopter rotor blade, Euler equations was solved numerically for simulating three-dimensional flowfield in the tip region. NACA0012 airfoil was used to show the changes of pressure contour on and around the wing surface, flow pattern in the tip region, and several aerodynamic coefficients along the spanwise direction due to various angles of attack and inflow velocities. Also to show the effect of rotating blade, the assumption of shear inflow model was used. The comparison of these results with and without wing tip shows the effects of the tip vortex on the flowfield. And as an advanced step to consideration of the more reliable method for a rotating effect, centripetal acceleration and Coriolis acceleration terms were added in the governing equations and solved in rotating coordinate system. The results were compared with those of fixed wing simulation.

3. Numerical Scheme

3.1. Governing Equations

In the generalized rotating coordinate system with angular velocity $\Omega = (0, -\Omega, 0)$, the three-dimensional, compressible, non-dimensionalized Euler equations concerning both Coriolis acceleration and centripetal acceleration effects can be written as

$$\frac{1}{J}\frac{\partial \mathbf{Q}}{\partial t} + \frac{\partial \hat{\mathbf{F}}}{\partial \xi} + \frac{\partial \hat{\mathbf{G}}}{\partial \eta} + \frac{\partial \hat{\mathbf{H}}}{\partial \zeta} + \frac{1}{J}\mathbf{T} = 0$$

where

$$\mathbf{Q} = [\rho, \rho u, \rho v, \rho w, e]^T,$$
$$\mathbf{F} = [\rho u, \rho u^2 + p, \rho uv, \rho uw, u(e+p)\ ]^T,$$
$$\mathbf{G} = [\rho v, \rho vu, \rho v^2 + p, \rho vw, v(e+p)\ ]^T,$$
$$\mathbf{H} = [\rho w, \rho wu, \rho wv, \rho w^2 + p, w(e+p)\ ]^T,$$
$$\hat{\mathbf{F}} = (\xi_x \mathbf{F} + \xi_y \mathbf{G} + \xi_z \mathbf{H})/J,$$
$$\hat{\mathbf{G}} = (\eta_x \mathbf{F} + \eta_y \mathbf{G} + \eta_z \mathbf{H})/J,$$
$$\hat{\mathbf{H}} = (\zeta_x \mathbf{F} + \zeta_y \mathbf{G} + \zeta_z \mathbf{H})/J$$
$$\mathbf{T} = [0, -\rho\Omega(\Omega x + 2w), 0, -\rho\Omega(\Omega z - 2u), 0]^T$$

In the above equations, ρ is the gas density, u, v, w the Cartesian velocity components in x, y, x directions respectively, and e the total energy per unit volume. The pressure is obtained by the perfect gas equation by

$$p = (\gamma - 1)\left[e - \frac{1}{2}\rho(u^2 + v^2 + w^2)\right]$$

The metric relations in three-dimensions are given by

$$\xi_x/J = y_\eta z_\zeta - y_\zeta z_\eta, \quad \xi_y/J = x_\zeta z_\eta - x_\eta z_\zeta,$$
$$\xi_z/J = x_\eta y_\zeta - x_\zeta y_\eta, \quad \eta_x/J = y_\zeta z_\xi - y_\xi z_\zeta,$$
$$\eta_y/J = x_\xi z_\zeta - x_\zeta z_\xi, \quad \eta_z/J = x_\zeta y_\xi - x_\xi y_\zeta,$$
$$\zeta_x/J = y_\xi z_\eta - y_\eta z_\xi, \quad \zeta_y/J = x_\eta z_\xi - x_\xi z_\eta,$$
$$\zeta_z/J = x_\xi y_\eta - x_\eta y_\xi$$

and the Jacobian of coordinate transformation, J, which is physically equivalent to the inverse of a cell volume, is defined by

$$J = [x_\xi(y_\eta z_\zeta - y_\zeta z_\eta) - x_\eta(y_\xi z_\zeta - y_\zeta z_\xi) + x_\zeta(y_\xi z_\eta - y_\eta z_\xi)\ ]^{-1}$$

The flux vectors can be written as

$$\hat{F},\hat{G},\hat{H}=\frac{|\nabla\kappa|}{J}\begin{bmatrix}\rho\bar{U}_\kappa\\ \rho\bar{U}_\kappa u+\hat{\kappa}_x p\\ \rho\bar{U}_\kappa v+\hat{\kappa}_y p\\ \rho\bar{U}_\kappa w+\hat{\kappa}_z p\\ \bar{U}_\kappa(e+p)\end{bmatrix},\quad \kappa=\xi,\eta,\zeta$$

where $\nabla\hat{\kappa}$ is the unit vector in the direction normal to the κ = constant coordinate surface

$$\nabla\hat{\kappa}=(\hat{\kappa}_x,\hat{\kappa}_y,\hat{\kappa}_z)=\frac{\nabla\kappa}{|\nabla\kappa|}=\frac{\nabla\kappa}{\sqrt{{\kappa_x}^2+{\kappa_y}^2+{\kappa_z}^2}}$$

and

$$U_\kappa=\hat{\kappa}_x u+\hat{\kappa}_y v+\hat{\kappa}_z w$$

is the contravariant velocity in the κ direction.

In the calculation with fixed wing, the angular velocity Ω was set to zero, so that the last term T in governing equations be also canceled.

3.2. Discretization

3.2.1. *Space discretization method*

The inviscid flux vectors are discretized using Roe's flux difference splitting (FDS) method [4] in which the flux difference across a cell interface is divided into components associated with each characteristic wave. By this method, the numerical flux in the x_i direction is expressed as

$$\hat{F}_{i+1/2}(Q_L,Q_R,\Gamma)=\frac{1}{2}\left[\hat{F}(Q_L,\Gamma)+\hat{F}(Q_R,\Gamma)-|\tilde{A}(\tilde{Q},\Gamma)|(Q_R-Q_L)\right]_{i+\frac{1}{2}}$$

where

$$|\tilde{A}_{i+1/2}|=\tilde{R}_{i+1/2}|\tilde{\Lambda}_{i+1/2}|\tilde{R}^{-1}_{i+1/2}$$

where Q_L and Q_R are the solution vectors extrapolated to the left and right sides of the cell interface. In the above, the columns of $\tilde{R}_{i+1/2}$ are the right eigenvectors of $\tilde{A}_{i+1/2}$ and the rows of $\tilde{R}^{-1}_{i+1/2}$ constitutes an orthonormal set of left eigenvectors. $|\tilde{\Lambda}_{i+1/2}|$ is the diagonal matrix of eigenvalues in absolute value with

$$\tilde{\Lambda}_{i+1/2}=\text{diag}\left[\tilde{U},\tilde{U},\tilde{U}+\tilde{c},\tilde{U}-\tilde{c}\right]_{i+1/2}\cdot\frac{|\nabla\kappa|}{J}$$

where the characteristic fields associated with the first and second eigenvalues are linearly degenerate and those associated with the other fields are genuinely nonlinear. Here, $\tilde{R}_{i+1/2}$, $\tilde{R}^{-1}_{i+1/2}$ and $|\tilde{\Lambda}_{i+1/2}|$ are evaluated with the ρ-averaged variables defined by

$$\begin{aligned}\tilde{\rho}&=\sqrt{\rho_L\rho_R}\\ \tilde{u}&=\frac{u_L\sqrt{\rho_L}+u_R\sqrt{\rho_R}}{\sqrt{\rho_L}+\sqrt{\rho_R}}\\ \tilde{v}&=\frac{v_L\sqrt{\rho_L}+v_R\sqrt{\rho_R}}{\sqrt{\rho_L}+\sqrt{\rho_R}}\\ \tilde{w}&=\frac{w_L\sqrt{\rho_L}+w_R\sqrt{\rho_R}}{\sqrt{\rho_L}+\sqrt{\rho_R}}\\ \tilde{H}&=\frac{H_L\sqrt{\rho_L}+H_R\sqrt{\rho_R}}{\sqrt{\rho_L}+\sqrt{\rho_R}}\\ \tilde{c}^2&=(\gamma-1)\left[\tilde{H}-\frac{1}{2}\left(\tilde{u}^2+\tilde{v}^2+\tilde{w}^2\right)\right]\end{aligned}$$

Unfortunately, Roe's approximate Riemann solver does not satisfy the entropy condition and thus permits physically inadmissible expansion shock. To remedy this problem, entropy correction is applied as

$$\left|\tilde{\lambda}_{i+1/2}\right|=\begin{cases}\left|\tilde{\lambda}_{i+1/2}\right| & \text{if } \left|\tilde{\lambda}_{i+1/2}\right|\geq\epsilon\\ \frac{\tilde{\lambda}^2_{i+1/2}+\epsilon^2}{2\epsilon} & \text{if } \left|\tilde{\lambda}_{i+1/2}\right|<\epsilon\end{cases}$$

where ϵ is a small nonnegative quantity which is determined by

$$\epsilon=\max\left[0,\left(\tilde{\lambda}_{i+1/2}-\lambda_i\right),\left(\lambda_{i+1}-\tilde{\lambda}_{i+1/2}\right)\right]$$

Since the entropy correction is required only for nonlinear fields, ϵ is set to zero for linear fields.

3.2.2. *Implicit method*

Space discretization of the governing equations provides a set of coupled ordinary differential equations

$$\frac{1}{J}\frac{dQ}{dt}=-R(Q)$$

where

$$\begin{aligned}R(Q)=&\left(\hat{F}-\hat{F}_\nu\right)_{i+1/2}-\left(\hat{F}-\hat{F}_\nu\right)_{i-1/2}\\ &+\left(\hat{G}-\hat{G}_\nu\right)_{i+1/2}-\left(\hat{G}-\hat{G}_\nu\right)_{i-1/2}\\ &+\left(\hat{H}-\hat{H}_\nu\right)_{i+1/2}-\left(\hat{H}-\hat{H}_\nu\right)_{i-1/2}\end{aligned}$$

Applying the backward Euler implicit time integration method to Eq.(28), one obtains

$$\frac{1}{J}\frac{\Delta Q}{\Delta t}=-R^{n+1}(Q)$$

where $\Delta Q^n=Q^{n+1}-Q^n$. The above equation is linearized in time about the known time level n using the Taylor series expansion and this leads to

$$\left[\frac{1}{J\Delta t}+\left(\frac{\partial R(Q)}{\partial Q}\right)\right]^n=-R(Q^n)$$

The governing equations are linearized in time following the same procedure as in two-dimensional equations and the resulting system is approximately factorized to simplify the solution procedure as

$$\left[\frac{1}{J\Delta t}+\delta_\xi\left(\frac{\partial \hat{F}}{\partial Q}\right)_i\right]^n\left[\frac{1}{J\Delta t}+\delta_\eta\left(\frac{\partial \hat{G}}{\partial Q}\right)_i\right]^n$$
$$\left[\frac{1}{J\Delta t}+\delta_\zeta\left(\frac{\partial \hat{H}}{\partial Q}\right)_i\right]^n\times\left(\frac{I}{J\Delta t}\right)^{-2}\Delta Q^n=-R^n(Q)$$

where

$$R^n(Q)=\left(\hat{F}-\hat{F}_\nu\right)^n_{i+1/2}-\left(\hat{F}-\hat{F}_\nu\right)^n_{i-1/2}$$
$$+\left(\hat{G}-\hat{G}_\nu\right)^n_{i+1/2}-\left(\hat{G}-\hat{G}_\nu\right)^n_{i-1/2}$$
$$+\left(\hat{H}-\hat{H}_\nu\right)^n_{i+1/2}-\left(\hat{H}-\hat{H}_\nu\right)^n_{i-1/2}$$

Then, the solution is obtained in the following sequence:

$$\left[\frac{1}{J\Delta t}+\delta_\xi\left(\frac{\partial \hat{F}}{\partial Q}\right)_i\right]^n\times\Delta Q^*=-R^n(Q)$$
$$\left[\frac{1}{J\Delta t}+\delta_\zeta\left(\frac{\partial \hat{G}}{\partial Q}\right)_i\right]^n\times\Delta Q^{**}=-R^*(Q)$$
$$\left[\frac{1}{J\Delta t}+\delta_\zeta\left(\frac{\partial \hat{H}}{\partial Q}\right)_i\right]^n\times\Delta Q^n=-R^{**}(Q)$$

$$Q^{n+1}=Q^n+\Delta Q^n$$

3.3. Grid System and Boundary Conditions

A generalized body-fitted curvilinear grid system was used with C-type mesh in the main flow direction. NACA0012 airfoil model was used as a blade sectional geometry.

For 3-dimensional fixed wing, these sectional mesh was extended in spanwise direction using H-type mesh. For 3-dimensional Rotary wing, it was bent to form a half cylinderical grid system, which is consistent with rotating coordinate system. To simulate the case with wing tip, the free-stream flow region as far as the length of wing span was added out of wing tip. All properties such as density, velocities, pressure are computed in the middle of each cell volumn to be a unstaggered grid system.

Boundary conditions have to be specified mainly in three parts: 1) wall boundary condition, 2) inflow condition and 3) outflow condition. On the surface of the wing, the normal component of the velocities were specified to be zero because of inviscid Euler equations, $(v_n)_{\text{wall}}=0$.

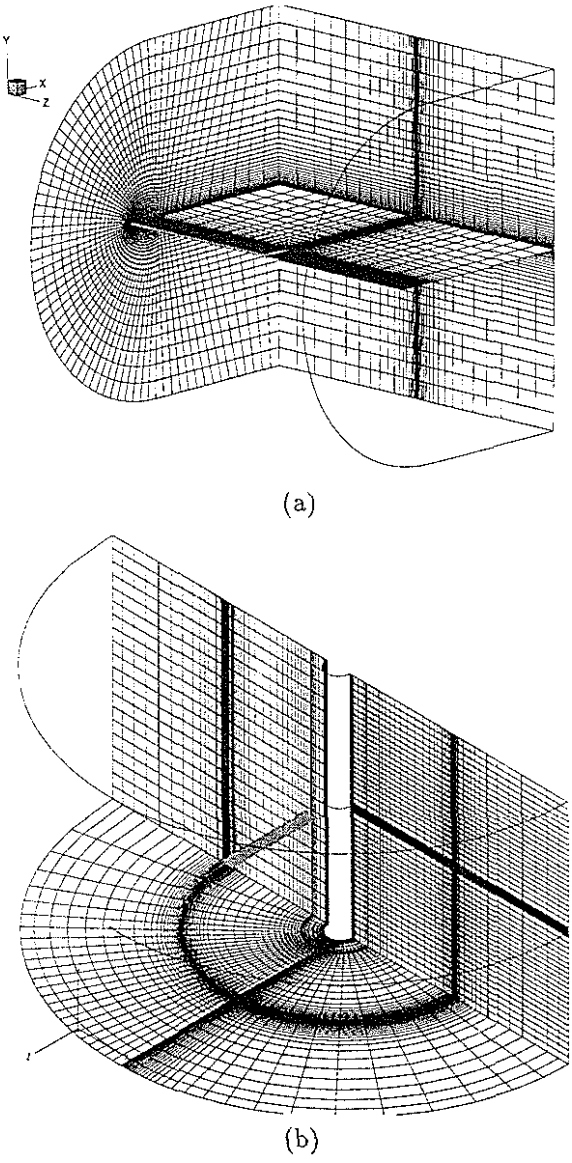

Fig.2: 3-dimensional grid systems for (a) fixed wing and (b) rotary wing

At the outflow boundaries, Riemann invariants condition was used as non-reflecting boundary condition, which prevented the outflow effects from entering into the computational region. Also at the far-field boundaries, which are as far as the spanwise length of blade span from the wing tip, normal conditions were used.

The C-grid system forms a cut behind the trailing edge of the blade and beyond the blade tip. Values along these branch-cut boundaries were obtained by simply overlapping the upper and lower grids to match the same properties. This may tend to diffuse the shed vorticity and other quantities behind the trailing edge, but with an adequately clustered grid, this diffusion may not be too much pronounced.

At the inflow bloundaries, the sevaral inflow conditions with various cases were used to simulate rotation of rotor.

With fixed wing, three different inflow models were

applied to show the factors which have an effect on rotor flow: (1) for the tip effects only, uniform free stream with Mach number to be 0.5, 0.6, 0.8 (Fig.3(a)), (2) for the rotor rotation only, the shear inflow condition with Mach number incresing linearly from root to wing tip without freestream region (0.15 to 0.6 and 0.2 to 0.8, Fig.3(b)), (3) for the combined effect of both tip effect and shear inflow effect, the same shear inflow models(0.6, 0.8 at tip) with freestream region (Fig3.(c))

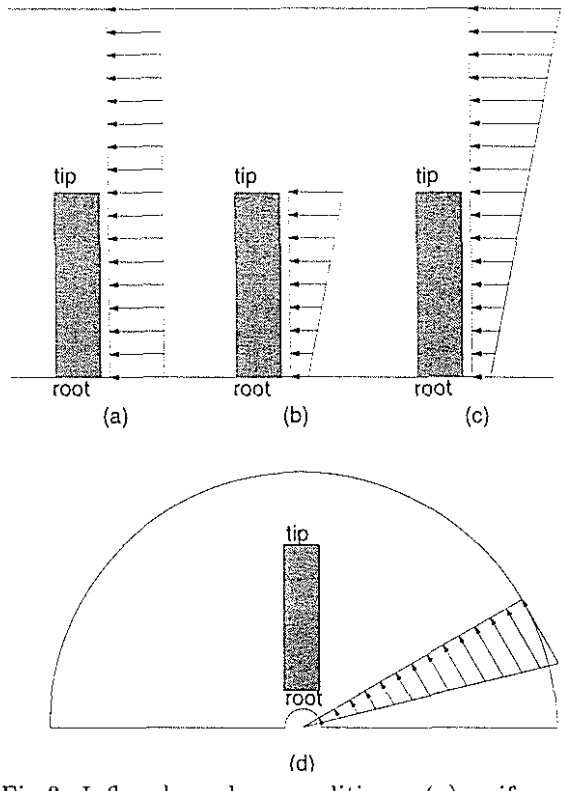

Fig.3: Inflow boundary conditions: (a) uniform with tip (b) shear without tip (c) shear with tip (d) rotary wing

With rotary wing, tip Mach number of the shear inflow condition coincided with the fixed wing at the value of 0.6, 0.8, as shown in Fig.3(d). In the region containing the blade root, two kinds of boundary conditions, normal or symmetric boundary condition, can be used; the former yieled better results, but this region was not so much dependent on boundary conditions, since the inflow velocity is relatively small.

4. Results and Discussions

The analysis with fixed wing was proceeded in three steps to show two typical effects by wing tip and rotor rotation. At first, uniform inflow was blown over the finite wing with tip to show the formation of a tip vortex, its roll-up feature and the change of the flow around tip. In the second step the shear inflow model without tip was applied to show the effect of rotation of helicopter rotor, where the shear inflow, a simple modeling of rotor rotation, means that the freestream Mach number of inflow increases along the spanwise direction linearly by the rotation of the blade. In the last step these two were combined to analize the whole effect of shear inflow over the wing with tip.

In case of rotary wing, the simulation of the rotation of rotor blade with the additional rotating effect, due to centripetal acceleration and Coriolis acceleration were solved and the results were compared with fixed wing.

4.1. Three steps for fixed wings

4.1.1. *Uniform inflow with wing tip*

To examine the wing tip effect, the flow around the wing was computed with freestream Mach numbers of Ma=0.5, 0.68 and 0.8 at angles of attack $\alpha = 0^o$ and 5^o. Figure 4 shows pressure contours on the upper and lower surfaces of the wing with a freestream Mach number Ma=0.8 at an angle of attack $\alpha = 5^o$. The higher pressure on the lower surface than that on the upper forms a lift force, and pressure distribution with a weak shock by the sudden increase of a local Mach number becomes smeared near the wing tip, approaching to a freestream. At least 3 chords from the wing tip, pressure distribution became similar with the 2-dimensional case.

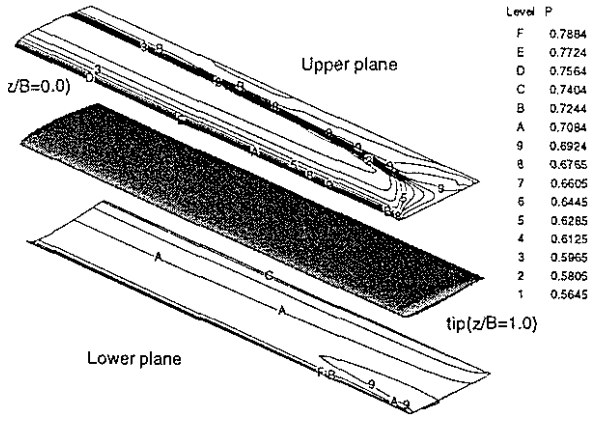

Fig.4: Pressure contours on upper and lower surfaces (Uniform Inflow with tip, $Ma_\infty = 0.8, \alpha = 5^o$)

The pressure contour at the chordwise cross-section shows an upward vortical flow pattern at the edge of the wing tip, which induces inward direction flow on the upper plate from the tip to root. The flow pattern near the tip region, fluid particles outside the tip runs into the wing, which is mixed with the flow over and under the wing surface to form a counter-clockwise tip vortex against the main flow direction and roll up to the downwards direction.

At the angle of attack $\alpha = 0^o$ with the assumption of inviscid flow, total lift and drag coefficients are all zero, and not only the flowfiled above and below the wing but also the tip vortex at downstream show symmetric patterns.

4.1.2. *Shear inflow without wing tip*

To examine the effect of the rotor rotation on the flow, the shear inflow model was used at angles of attack 0 and 5 . The shear inflow model of rotor rotation was specified in two cases: the case where Mach number increses linearly to be from 0.15 at root to 0.6 at tip and from 0.2 to 0.8. To show the sole effect of the rotation of rotor, the Neumann boundary condition was used at both root and tip. Figure 5 shows pressure contours on the upper and lower surfaces of the wing with a freestream Mach number Ma=0.8 at an angle of attack $\alpha = 5^o$. Dissimilarly with 2-dimensional results, the result with shear inflow shows induced flow along the span from the region with a higher inflow velocity to the one with lower velocity, i.e. from tip to root.

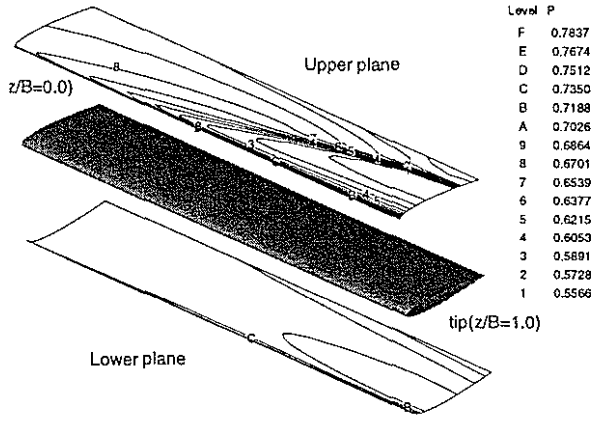

Fig.5: Pressure contour on upper and lower surfaces (Shear without tip, $Ma_{\text{tip}} = 0.8, \alpha = 5^o$)

4.1.3. *Shear inflow with wing tip*

Two effects used in the previous steps, tip effect and shear inflow, are combined as a simple model of a rotating helicopter roter blade at angles of attack $\alpha = 0^o$ and 5^o. The geometry and the shear inflow conditions simulating the rotation of the rotor are the same as the previous cases. The freestream Mach number of shear inflow was specified to the same values with the case of shear inflow without tip for comparision: the one of Mach number 0.6 at tip and the other, 0.8. Figure 6 shows pressure contours on the upper and lower surfaces of the wing with a freestream Mach number of 0.8 at an angle of attack $\alpha = 5^o$. Compared with the case of the simple shear inflow condition, the contours show not so much pressure variation along the span in the tip region, approaching to the freestream flow region. The pressure jump like a shock by an increase of the local Mach number also gradually decreases to be uniform pressure distribution to enter the freestream flow region. The shear inflow effect in the front part of the blade upper surface is dominated by the tip effect of the induced w-velocity into the root along the spanwise direction. It means that in the rear part of the blade surface and downstream flow region the tip effect becomes dominant.

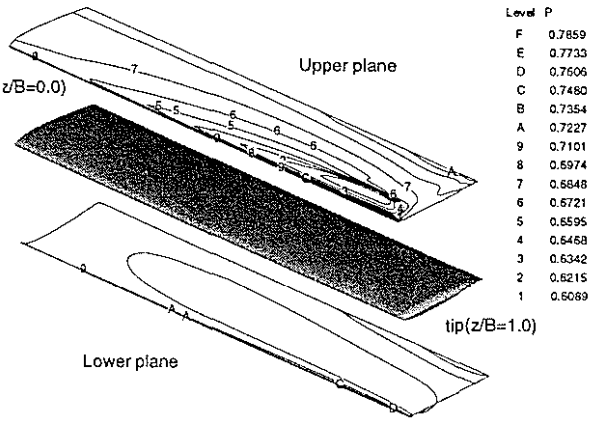

Fig.6: Pressure contour on upper and lower surfaces (Shear Inflow with tip, $Ma_{\text{tip}} = 0.8, \alpha = 5^o$)

4.1.4. *Comparison of lift coefficients*

Figure 7 shows the profiles of a lift coefficient(C_l) of three steps at each cross-section along spanwise direction with a corresponding freestream Mach numbers an angle of attack $\alpha = 5^o$.

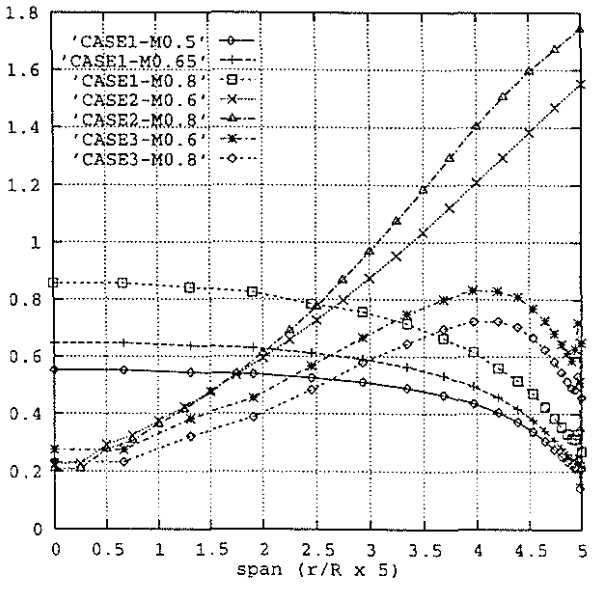

Fig.7: Lift coefficient comparision in each cases

For the case of uniform inflow with tip, as Mach number increases these coefficients increase in the whole field, and the decreasing tendency along span is also shown as approaching the freestream region. At the root region the profile of lift coefficients is similar to 2-dimensional computed and experimental data.

In the case of shear inflow without tip, increasing Mach number along the span increases the sectional lift coefficient. In addition, the w-velocity caused by the shear inflow makes the flowfield entirely different from 2-dimensional one. The flow induced by the shear inflow increases the pressure in root region and decreases the pressure near tip region. This effect

makes a higer lift in the tip region and lower lift in root region than 2-dimensional computed data where the lift shows smooth increase with Mach number. That is to say, the induced flow by the rotor rotation causes the sectional lift and drag coefficients to have more steep slopes than 2-dimensional results.

The case of shear inflow with tip, increasing inflow velocity along the span by the shear inflow increases the lift, but near the tip the tip effect reduces the lift. In the result the profiles show the pattern as is in the figure: the local lift coefficients with the freestream Mach number at tip 0.6, are larger in all region than those of 0.8, which is contrary of the fact that lift coefficient increases with incresing Mach number. This can be explained by the fact that the relatively smaller lift coefficient at the blade root for $Ma_{\text{tip}}=0.8$ by the effect of shear inflow cannot restore the lift. Increasing Mach number along the span dosen't grow enough to catch up the case for $Ma_{\text{tip}}=0.6$ on account of tip effect which pulls down the lift coefficients along the span, especially in the tip region.

4.2. Shear Inflow with rotary wings

The flowfield around the rotor blade in rotating coordinate system is similar to that of shear inflow with tip at fixed wing, but the induced velocity against the spanwise direction pulls the conter of tip vortex to the root, i.e. rotating axis.

Figure 8 shows the pressure contours on the upper and lower surfaces of the rotary wing with freestream Mach number $Ma=0.8$ at an angle of attack $\alpha=5^o$. Contours are very similar with those of shear inflow model with fixed wing tip. The pressure difference between upper and lower surfaces produces a lift force and the efftect of shear flow and tip effect are shown in the contours.

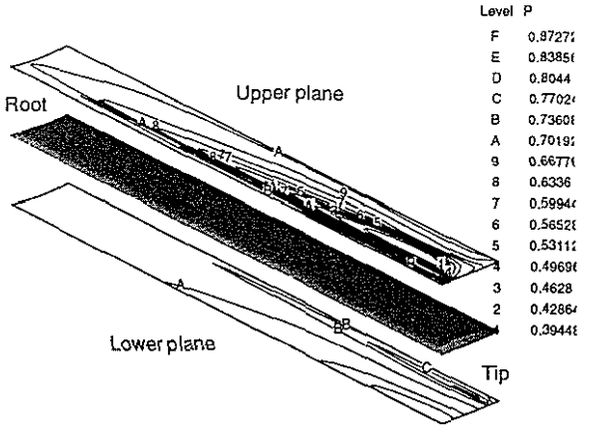

Fig.8: Pressure contour on upper and lower surfaces (Rotary wing, $Ma_{\text{tip}}=0.8, \alpha=5^o$)

Figure 9 shows the Mach number contour of the upper surface of the rotor wing. The pressure jump like a shock by an increase of the local Mach number also gradually decreases to be uniform pressure distribution to enter the freestream flow region.

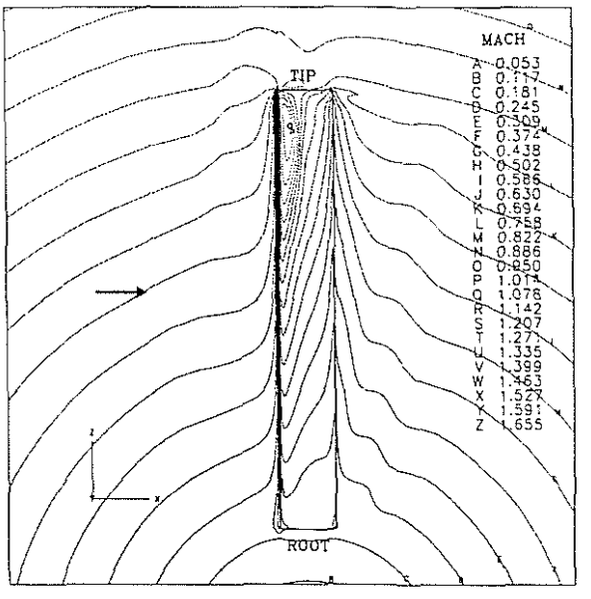

(a)

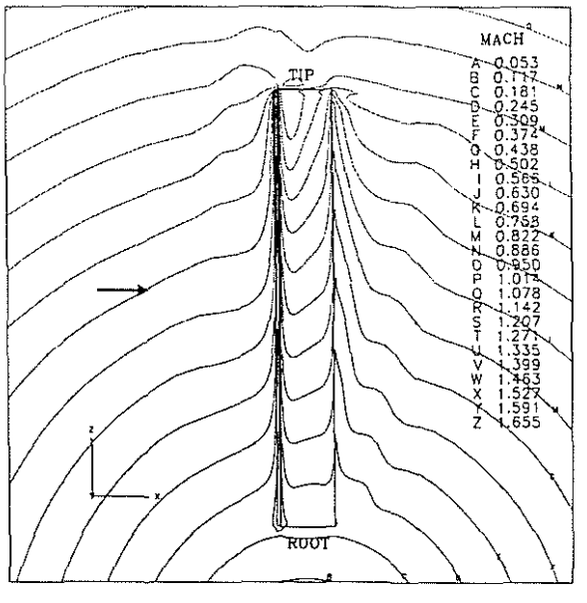

(b)

Fig.9: Mach number contour on the surfaces with rotary wing ($Ma_{\text{tip}}=0.8, \alpha=5^o$): (a) lower surface (b) upper ssurface

Figure 10 shows the v-velocity contour near the rotor blade. Along the chordwise stream, the center tip vortex, which can be seen in v-velocity contour figure as a large gradient values, was pulled into the root. It shows, so called, the contraction of the tip vortex.

Figure 11 shows the pressure coefficients along spanwise direction near the tip region with both fixed and rotary wings with freestream Mach number $Ma=0.8$

at an angle of attack $\alpha = 5^o$. Due to the incresing inflow velocity along the span by the rotation of the rotor, sectional C_p shows gradually large gradient, and this causes the shock on the upper surface in some region. But as closer to tip, tip effect become more dominant to decrease the pressure gradient to enter the freestream region.

As the whole comparison of the results between the fixed wing and rotary wing with freestream Mach number $Ma = 0.6, 0.8$ at an angle of attack $\alpha = 5^o$, the lift coefficients was plotted in figure 12.

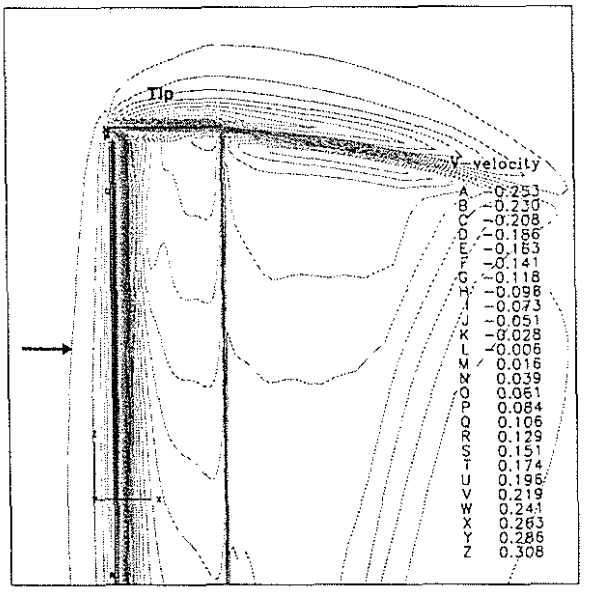

Fig.10: V-velocity contour on the upper surface with rotary wing ($Ma_{tip} = 0.8, \alpha = 5^o$)

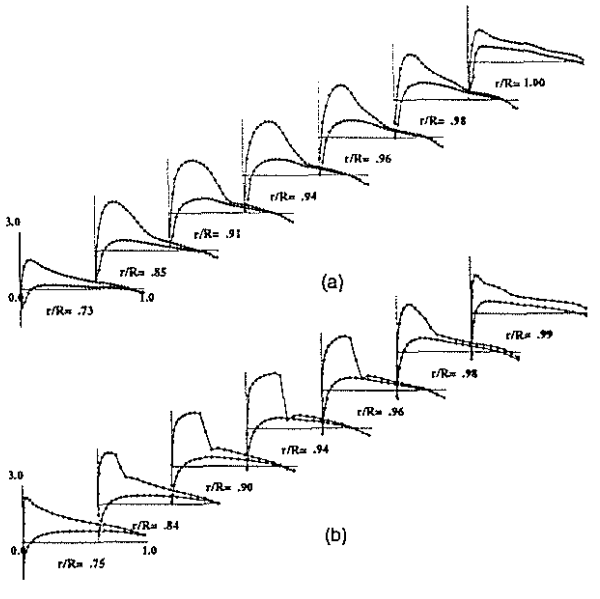

Fig.11: Pressure coefficient along the span: (a)rotary wing (b) fixed wing

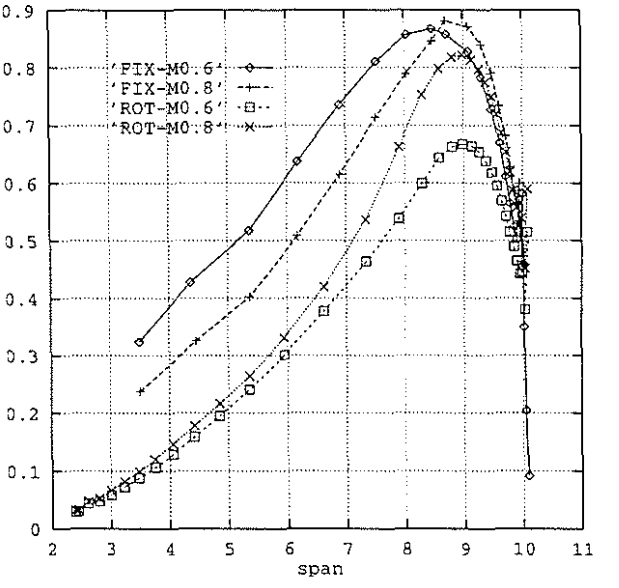

Fig.12: Lift coefficient comparision in each cases

5. Conclusion

A flow solver has been developed to solve the three-dimensional, compressible flow around a helicoter rotor blade with the inviscid Euler equations. A linear shear inflow along the spanwise direction was used as a model for rotation effect.

The flows around the fixed wing were analyzed using different inflow boundary conditions step by step to see the tip effect ,the rotation effect and combined effects respectively. The conclusions of three cases for fixed wing are the followings.

(1) A tip effect pulls down the local lift coefficients to be finally zero as approaching the wing tip, then freestream region begins. The flow passing by the tip forms a tip vortex and rolls up along the downward direction.

(2) A shear inflow brings about the increase of lift coefficients in virtue of increasing inflow-velocity along the wing span. It also induces the w-velocity against the spanwise direction, which reduces the lift coefficients near the root region and enlarges near the tip region.

(3) In the case of shear inflow with tip, the tip effect and shear inflow effect are ovelapped each other. The shear inflow effect are dominant in the root region and in the front part of the blade, on the other hand, the tip effect is dominant in the tip region and in the downstream of the blade.

The case of rotary wing with rotating coordinate system shows more realistic flowfield of hovering helicopter, especially at the trace of tip vortex.

REFERENCES

G. R. Srinivasan, W. J. McCroskey, J. D. Baeder and T. A. Edwards, "Numerical Simulation of Tip Vortices of Wings in Subsonic and Transonic Flows", *AIAA Journal*, Vol.26, Oct. 1988, pp. 1153-1162

P. L. Roe, "Approximate Riemann Solvers, Parameter Vectors and Difference Schemes", *Journal of Computational Physics*, Vol. 43, 1981, pp. 357-372

Bram van Leer, "Flux-Vector Splitting For The Euler Equations", *Lecture Notes on Physics*, Vol. 170, 1982, pp. 507-512

L. E. Eriksson, "Generation of Boundary-Conforming Grids Around Wing-Body Configurations Using Transfinite Interploation", *AIAA Journal*, Vol.20, Oct. 1982, pp. 1313-1320

James L. Thomas and M. D. Salas, "Far-Field Boundary Conditions for Transonic Lifting Solutions to the Euler Equations", *AIAA Journal*, Vol.24, No.7, 1986, pp.1074-1080

N. N. Mansour, "Numerical Simulation of the Tip Vortex Off a Low-Aspect Ratio Wing at Transonic Speed", *AIAA Journal*, Vol.23, Aug. 1985, pp. 1143 -1149

U. Kaynak, T. Holst, B. J. Cantwell and R. L. Sorenson, "Numerical Simulation of Transonic Seperated Flows over Low-Aspect Ratio Wings", *Journal of Aircraft*, Vol.24, Aug. 1987, pp. 531-539

Thomas H. Pulliam and Joseph L. Steger, "Implicit Finite-Difference Simulations of Three-Dimensional Compressible Flow", *AIAA Journal*, Vol.18, No.2, Feb. 1980, pp. 159-167

R. K. Agarwal and J. E. Deese, "Euler Calculations for Flowfield of a Helicopter Rotor in Hover", AIAA Paper 86-1782, pp.425-433

Takashi Aoyama, Shigeru Saito and Keiji Kawachi, "Navier-Stokes Analysis of Blade Tip Shape in Hover", 16th European Rotorcraft Forum, 1990

J. Bosschers, B. Montgomerie, A. J. Brand and R. P. J. O. M. van Rooy, "Influence of Blade Rotation on the Sectional Aerodynamics of Rotating Blades", 22nd European Rotorcraft Forum, 1996

Brian E. Wake, "Solution Procedure for the Navier-Stokes Equations Applied to Rotors", Ph.D Thesis, Georgia Institute of Technology, 1987

J. Katz and A. Plotkin, Low-Speed Aerodynamics - From Wing Theory to Panel Methods, McGraw-Hill Inc., pp. 331-342

I. H. Abbott and A. E. von Doenhoff, Theory of WIng Section, Dover Publications Inc.